

# General Theory of Holographic Inversion With Linear Frequency Modulation Radar and Its Application to Whole-Body Security Scanning

Yang Meng<sup>D</sup>, Chuan Lin<sup>D</sup>, Member, IEEE, Jiefeng Zang, Anyong Qing, Senior Member, IEEE,  
and Natalia K. Nikolova<sup>D</sup>, Fellow, IEEE

**Abstract**—We present a general theory of the holographic image reconstruction with linear frequency modulation (LFM) radars. For the first time, the system limitations in terms of the object extent and distance are derived and explicitly related to the LFM radar frequency-modulation slope  $\gamma$ . The holographic inversion formula is improved to account for the spherical spread of the scattered wave. The theory and the generalized holographic inversion algorithm are validated by synthetic benchmark data as well as experimental data from an in-house LFM-radar prototype operating at 29.9-GHz central frequency and bandwidth of 5.8 GHz. Experiments confirm that the lateral spatial resolution is about 5 mm. For optimal performance, the system is calibrated using a simple but effective calibration approach based on a measurement with a metallic plate. Experiments, with a volunteer carrying metallic and nonmetallic objects, demonstrate very good performance in realistic scenarios.

**Index Terms**—Holographic inversion, linear frequency modulation (LFM), millimeter wave radar, security scanning.

## I. INTRODUCTION

ENSURING the public safety is challenging in a world of ever growing human traffic and increasing armed violence. Security inspection is now a commonplace, and a great variety of imaging and detection devices are deployed [1] at airports, major transportation hubs, places of entertainment,

Manuscript received June 30, 2020; accepted July 22, 2020. Date of publication August 21, 2020; date of current version November 4, 2020. This work was supported in part by the National Key Research and Development Plan under Grant 2018YFC0809500; in part by National Young Thousand Talent under Grant A0920502051826, Grant YH199911041801, and Grant YX1199912371901; in part by Foreign Talent in Culture and Education under Grant 110000207520190055; and in part by the Fundamental Research Funds for the Central Universities under Grant 2682018CX20.

Yang Meng is with the School of Physics, University of Electronic Science and Technology of China, Chengdu 610054, China (e-mail: mengyang@std.uestc.edu.cn).

Chuan Lin is with the School of Electrical Engineering, Southwest Jiaotong University, Chengdu 610031, China (e-mail: lin\_langai@163.com).

Jiefeng Zang is with the School of Physical Science and Technology, Southwest Jiaotong University, Chengdu 610031, China (e-mail: zjf\_max@126.com).

Anyong Qing is with the School of Electrical Engineering, Southwest Jiaotong University, Chengdu 611756, China, and also with the School of Physics, University of Electronic Science and Technology of China, Chengdu 610054, China (e-mail: qinganyong@tsinghua.org.cn).

Natalia K. Nikolova is with the Department of Electrical and Computer Engineering, McMaster University, Hamilton, ON L8S 4K1, Canada (e-mail: nikolova@ieee.org).

Color versions of one or more of the figures in this article are available online at <http://ieeexplore.ieee.org>.

Digital Object Identifier 10.1109/TMTT.2020.3016323

government centers, and military bases. The goal is to prevent prohibited items (e.g., weapons and explosives) from being smuggled into sensitive installations or crowded public areas and vehicles, where civilians are easy targets.

There are many methods for security inspection and surveillance [1]–[3], ranging from traditional security presence (e.g., police personnel and dogs) through handheld and walk-through metal detectors [4] to sophisticated whole-body scanners (millimeter-wave and X-ray) and emerging radars for concealed weapon detection (CWD) on moving people [5].

Metal detectors are incapable of detecting plastics, liquids, and ceramics, which materials are often found in explosive devices, handheld weapons, and contraband items. However, nonmetallic objects are detectable by technologies that use higher frequencies such as millimeter waves, infrared, and X-rays. Unfortunately, the infrared technology [4], [7] suffers from the poor penetration through thick clothing, whereas X-ray imagers use ionizing radiation, which is not suitable for deployment in public areas due to health hazards.

Millimeter waves, on the contrary, are safe (nonionizing) and they penetrate through clothing well. This has made the technology dominant in applications for partial or whole-body imaging [8]–[15]. It has been commercialized [16]–[20] and is currently used at major airports around the world.

Holographic image reconstruction is arguably the most effective processing algorithm for active millimeter-wave whole-body security inspection. Heterodyne mixing allows for acquiring both amplitude and phase information. Holography is capable of providing both 2-D and 3-D images of the body in real time. Its principles were developed originally for applications in microscopy [21], [22] and later extended to acoustic [23] and microwave [24], [25] imaging.

Other methods for image processing with millimeter waves are also the subject of intense research. Back projection (BP) algorithms have been proposed for millimeter-wave security inspection [26]–[30]. These algorithms meet the high-resolution requirements for security inspection; however, they have high computational complexity. With the aid of fast Fourier transform (FFT), this complexity can be reduced [31], but real-time imaging remains a challenge. Time-domain reflectometry (TDR) algorithms [32] have also been introduced. They also face the problem of computational efficiency.

The method discussed here belongs to the category of holographic imaging, which was introduced by Sheen *et al.* [13], [14] for imaging with monostatic data on planar and cylindrical surfaces. It has been further developed to process multistatic far-zone data [33]–[36]. Numerous developments followed, of which we mention only those closely related to the results presented here. Zhuge and Yarovoy [37] designed a sparse multiple-input multiple-output-synthetic aperture radar (MIMO-SAR) imaging system for CWD, combining the advantages of SAR reconstruction (akin to holography) and MIMO technology. Subsequently, they proposed a 3-D algorithm [38], suitable for measurements at closer range (the Fresnel region), by considering the spherical wavefronts of both the incident and scattered fields. Gao *et al.* [39], [40] proposed highly efficient 3-D algorithms for MIMO arrays in planar and cylindrical configurations with far-zone data. Yanik and Torlak [41] combined the SAR method with sparse MIMO arrays to achieve optimal compromise between short data acquisition time and low complexity. Amineh *et al.* [43], [44] proposed holographic algorithms for imaging at very close range (reactive near and Fresnel regions) for applications in medical imaging and nondestructive testing [44], [45]. Notably, the algorithm avoids interpolation in  $k$ -space, improving accuracy, and reducing computations. They also formulated holography in terms of the system point spread function (PSF), which, when measured, enables quantitative imaging in real time [46], [47].

Most of the above work assumes step-frequency measurements, which are time-consuming and expensive [48], especially with a large number of frequency samples within a wide band. Linear frequency modulation (LFM) radars offer an attractive alternative, especially in millimeter-wave imaging [48]–[50], [53], due to the lower cost and faster acquisition. Bleh *et al.* [51] designed a W-band frequency modulated continuous wave (FMCW) MIMO radar for far-field 3-D imaging with a BP algorithm. Nan *et al.* [52] proposed a generalized continuous-wave SAR (GCW-SAR) method that uses deramp-on-receive and piecewise constant Doppler (PCD) reconstruction. Its advantage is that it is applied easily with existing FMCW radars. Sheen *et al.* [9], [14], [54] and Sheen and Hall [33] also employed linear FMCW (LFMCW) radar to perform holographic imaging. Therein, heterodyne mixing leads to an intermediate frequency (IF) version of the LFM signal, which is processed using the classic scattering model of a superposition integral over the target reflectivity multiplied by the round-trip phase delay. While this model allows for the use of the same reconstruction formula as in stepped-frequency radars, it is subject to limitations which, to our knowledge, have not been rigorously analyzed.

Here, we focus on the LFM signal processing in holographic reconstruction with two new developments. First, we generalize the scattering model to accommodate the spherical amplitude spread of the scattered signal, which improves the image quality in the close-range application of whole-body scanning. Second, we develop a rigorous mathematical model of the received de-chirped LFM signal with explicit second-order phase-delay terms. We analyze the effect of neglecting these terms when the stepped-frequency holographic reconstruction formula is used directly. The analysis

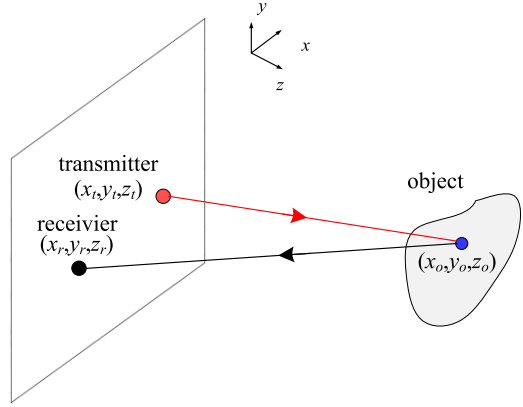


Fig. 1. Configuration of the planar holographic imaging system.

states explicitly the limitations in object zone and reference distance to radar in terms of the LFM frequency modulation slope  $\gamma$ .

It is also worth noting that, traditionally, the LFM signal processing requires the suppression of the Doppler effect and the residual video phase error (i.e., the second-order phase-delay error) with matched filtering [55], or polar formatting and subaperture techniques, or the deskew operation [56], [57]. In contrast, our reconstruction procedure processes the down-converted Fourier-transformed LFM signal directly with negligible errors, which is ensured by the proper choice of the frequency modulation slope  $\gamma$  as related to the distance to target and the target extent.

We refer to the proposed reconstruction procedure as generalized holographic inversion with LFM (GHI-LFM). The algorithm is integrated with a Ka-band in-house prototype [58] to validate and test its performance in realistic whole-body security screening scenarios. We report a simple but effective method for calibrating the system using measurement of a metallic screen. The results of experiments with benchmark targets as well as volunteers carrying various metallic and nonmetallic objects under jackets are reported. The results validate the expected spatial resolution of the images and confirm the system suitability for security screening.

The GHI-LFM algorithm is derived in Section II. Section III provides the algorithm limitation, performance comparison with prior work, and robustness analysis with synthetic benchmark data. The in-house prototype for human-body security screening is briefly introduced in Section IV along with the method used to calibrate it. Experimental validations are given in Section V, and Section VI provides discussion and conclusions.

## II. THEORY

A setup for planar imaging is illustrated in Fig. 1. The target is represented by its reflectivity  $\sigma(\mathbf{r}_o)$ , where  $\mathbf{r}_o = (x_o, y_o, z_o)$  is a point within the imaged object,  $\mathbf{r}_r = (x_r, y_r, z_r)$  is the location of the receiver, and  $\mathbf{r}_t = (x_t, y_t, z_t)$  is that of the transmitter.

### A. Holography With Account for Spherical Spread

The bistatic echo signal  $s(\mathbf{r}_r, \mathbf{r}_t, k)$  is

$$s(\mathbf{r}_r, \mathbf{r}_t, k) = \iiint \sigma(\mathbf{r}_o) \frac{\exp(-ikR_{to}) \cdot \exp(-ikR_{or})}{R_{or}} d\mathbf{r}_o \quad (1)$$

where  $i = \sqrt{-1}$ ,  $k = \omega/c$  is the wave number,  $\omega$  is the radian frequency, and  $c$  is the speed of light. The distances from the transmitter to the target and from the target to the receiver are, respectively,

$$R_{\text{to}}(\mathbf{r}_o) = \sqrt{(x_o - x_t)^2 + (y_o - y_t)^2 + (z_o - z_t)^2} \quad (2)$$

$$R_{\text{or}}(\mathbf{r}_o) = \sqrt{(x_r - x_o)^2 + (y_r - y_o)^2 + (z_r - z_o)^2}. \quad (3)$$

Note that the time factor  $e^{-i\omega t}$  is assumed and suppressed. Also, the model in (1) assumes that only the scattered signal has a spherical wavefront. Formulation for the case of spherical wavefronts for both the incident and the scattered waves is also possible, see [38]. For simplicity, let us assume monostatic measurements where (1) becomes

$$s(\mathbf{r}, k) = \iiint \sigma(\mathbf{r}_o) \frac{\exp(-i2kR)}{R} d\mathbf{r}_o \quad (4)$$

with  $\mathbf{r} = (x, y, z) = \mathbf{r}_r = \mathbf{r}_t$ ,  $R = R_{\text{to}} = R_{\text{or}}$ .

As per Weyl's identity [59]–[61]

$$\frac{\exp(-i2kR)}{R} = \frac{1}{2\pi} \int_{-\infty}^{\infty} \int_{-\infty}^{\infty} \frac{\exp(-ik_z|z_o - z|)}{ik_z} \cdot \exp[-ik_x(x_o - x) - ik_y(y_o - y)] dk_x dk_y \quad (5)$$

where

$$(2k)^2 = k_x^2 + k_y^2 + k_z^2. \quad (6)$$

Now, (4) can be represented as

$$s(\mathbf{r}, k) = \frac{1}{2\pi} \int_{-\infty}^{\infty} \int_{-\infty}^{\infty} \frac{F(k_x, k_y, k_z) \cdot \exp(ik_z z)}{ik_z} \cdot \exp[i(k_x x + k_y y)] dk_x dk_y \quad (7)$$

where  $F(k_x, k_y, k_z)$  is the Fourier transform of the reflectivity

$$F(k_x, k_y, k_z) = \iiint \sigma(\mathbf{r}_o) \cdot \exp[-i(k_x x_o + k_y y_o + k_z z_o)] d\mathbf{r}_o. \quad (8)$$

From (7), it follows that

$$F(k_x, k_y, k_z) = \frac{ik_z \exp(-ik_z z)}{2\pi} S(k_x, k_y, k_z) \quad (9)$$

where

$$S(k_x, k_y, k_z) = \int_{-\infty}^{\infty} \int_{-\infty}^{\infty} s(\mathbf{r}, k) \cdot \exp(-ik_x x - ik_y y) dx dy. \quad (10)$$

Note that (9) requires the re-sampling of  $S(k_x, k_y, k_z)$  using (6), which maps the coordinates  $(k_x, k_y, k_z)$  onto the coordinates  $(k_x, k_y, k_z)$ . The resulting data set is given by  $S(k_x, k_y, k_z)$ . Finally, the reflectivity is retrieved from (9) by

$$\sigma(\mathbf{r}_o) = \text{FT}_{3D}^{-1} \left[ S(k_x, k_y, k_z) \cdot \frac{ik_z \exp(-ik_z z)}{2\pi} \right] \quad (11)$$

where  $\text{FT}_{3D}^{-1}$  denotes the 3-D inverse Fourier transform. In essence, (11) is an enhancement of the classic holographic inversion formula, see [13, eq. (23)], to take into account the free-space magnitude decay associated with the spherical spread of the backscattering. Improvement in the reconstruction is expected due to this enhancement, especially in close-range measurements (see Sections III-C and III-D).

## B. Holography With LFM

1) *Transmitted LFM Signal:* The transmitted LFM signal is given by

$$s_t(\hat{t}, t_m) = P\left(\frac{\hat{t}}{T_P}\right) \cdot \exp\left[i2\pi\left(f_c t + \frac{1}{2}\gamma \hat{t}^2\right)\right] \quad (12)$$

where  $t$  is time,  $\hat{t} = t - t_m$  is the fast time,  $t_m = mT$  ( $m = 0, 1, 2, \dots$ ) is the slow time,  $T$  is the period,  $T_P$  is the pulse width,  $T_P < T$ ,  $f_c$  is the center frequency,  $\gamma$  is the frequency-modulation slope, and  $P$  denotes the rectangular pulse function

$$P(u) = \begin{cases} 1, & |u| \leq 1/2 \\ 0, & \text{otherwise.} \end{cases} \quad (13)$$

2) *Received LFM Signal:* Up to a multiplicative factor, the received LFM signal can be represented as

$$s_r(\mathbf{r}_r, \hat{t}, t_m) = \iiint \frac{\sigma(\mathbf{r}_o)}{R(\mathbf{r}_o)} \cdot P\left(\frac{\hat{t} - t_{\text{tor}}}{T_P}\right) \cdot \exp\left\{i2\pi\left[f_c(t - t_{\text{tor}}) + \frac{1}{2}\gamma(\hat{t} - t_{\text{tor}})^2\right]\right\} d\mathbf{r}_o \quad (14)$$

where  $t_{\text{tor}}(\mathbf{r}_o)$  is the signal travel time along the path transmitter-object-receiver

$$t_{\text{tor}} = (R_{\text{to}} + R_{\text{or}})/c = 2R/c. \quad (15)$$

3) *Dechirping of the Received LFM Signal:* The dechirp processing works on the time-dependent terms in the integrand of (14)

$$s_r(\hat{t}, t_m) = P\left(\frac{\hat{t} - t_{\text{tor}}}{T_P}\right) \cdot \exp\left\{i2\pi\left[f_c(t - t_{\text{tor}}) + \frac{1}{2}\gamma(\hat{t} - t_{\text{tor}})^2\right]\right\}. \quad (16)$$

It mixes the reference signal with the received one to get the IF echo signal

$$s_{\text{IF}}(\hat{t}, t_m) = s_r(\hat{t}, t_m) \cdot s_{\text{ref}}^*(\hat{t}, t_m) \quad (17)$$

where the superscript \* stands for complex conjugate, and

$$s_{\text{ref}}(\hat{t}, t_m) = P\left(\frac{\hat{t} - t_{\text{ref}}}{T_{\text{ref}}}\right) \cdot \exp\left\{i2\pi\left[f_c(t - t_{\text{ref}}) + \frac{1}{2}\gamma(\hat{t} - t_{\text{ref}})^2\right]\right\}. \quad (18)$$

Here,  $t_{\text{ref}}$  is the signal travel time from the transmitter to the reference position and on to the receiver. The reference position is usually chosen at the center of the anticipated object zone

$$t_{\text{ref}} = (R_{tc} + R_{cr})/c = 2R_{\text{ref}}/c \quad (19)$$

with  $R_{tc}$  and  $R_{cr}$  being the distances from the transmitter to the center of the zone and that from the center to the receiver ( $R_{tc} = R_{cr} = R_{\text{ref}}$  in the monostatic case). We also introduce the pulse width  $T_{\text{ref}}$  of the reference signal defined as

$$T_{\text{ref}} = T_P + 2\Delta o/c \quad (20)$$

where  $\Delta o$  is the anticipated extent of the object.

The substitution of (16) and (18) into (17) gives the IF signal model

$$s_{\text{IF}}(\hat{t}, t_m) = A \cdot P \left( \frac{\hat{t} - t_{\text{tor}}}{T_p} \right) \cdot \exp[i2\pi(t_{\text{ref}} - t_{\text{tor}})(f_c + \gamma \hat{t})] \cdot \exp[-i\pi\gamma(t_{\text{ref}} + t_{\text{tor}})(t_{\text{ref}} - t_{\text{tor}})] \quad (21)$$

where  $A$  is the amplitude. In each period of the LFM signal, the slow time  $t_m$  remains constant and has no relation to the object and so it is omitted hereafter. Further, let

$$\Delta t = t_{\text{tor}} - t_{\text{ref}} = 2(R - R_{\text{ref}})/c = 2\Delta R/c. \quad (22)$$

The IF signal can then be expressed as

$$s_{\text{IF}}(\hat{t}) = A \cdot P \left( \frac{\hat{t} - t_{\text{tor}}}{T_p} \right) \cdot \exp(-i2\pi f_c \Delta t) \cdot \exp[-i2\pi\gamma(\hat{t} - t_{\text{ref}})\Delta t] \cdot \exp[i\pi\gamma(\Delta t)^2]. \quad (23)$$

In (23), the second and third exponential terms are the second-order range and phase-delay terms, respectively.

To process the IF signal in the frequency domain, Fourier transform with respect to  $\hat{t}$  is applied. Therefore, (23) is expressed as

$$S_{\text{IF}}(f) = A \cdot \exp[-i2\pi f_c \Delta t + i2\pi\gamma t_{\text{ref}} \Delta t + i\pi\gamma(\Delta t)^2] \cdot \int_{-\infty}^{\infty} P \left( \frac{\hat{t} - t_{\text{tor}}}{T_p} \right) \cdot \exp(-i2\pi\gamma\Delta t \cdot \hat{t}) \cdot \exp(-i2\pi f \cdot \hat{t}) d\hat{t} \quad (24)$$

the solution of which is a narrow *sinc* shaped pulse:

$$S_{\text{IF}}(f) = A \cdot T_p \cdot \exp[-i2\pi f_c \Delta t + i2\pi\gamma t_{\text{ref}} \Delta t + i\pi\gamma(\Delta t)^2] \cdot \text{sinc}[T_p(f + \gamma \Delta t)] \cdot \exp[-i2\pi(f + \gamma \Delta t)t_{\text{tor}}]. \quad (25)$$

Thus, the echo signal from a point scatterer is modeled as a very narrowband signal, the central frequency of which is proportional to the distance between this scatterer and the reference point (the center of the object):  $f_s = -\gamma \Delta t$  or  $f_s = -\gamma 2\Delta R/c$ .

The careful examination of the signal in (25) reveals that it cannot be used directly as an input to the holographic inversion formula in (11). First, it depends on the chosen reference point through the reference time  $t_{\text{ref}}$  and through  $\Delta t = t_{\text{tor}} - t_{\text{ref}}$ ; see (22). Second, the phase spectrum at  $f_s$ , where the *sinc* function peaks, is *not* proportional to the time of flight  $t_{\text{tor}} = 2R/c$  (or the distance to the point scatterer  $R$ ). A signal, which can be directly processed by holographic inversion (as described in the next subsection) must have the form

$$S'_{\text{IF}}(f) = A \cdot T_p \cdot \text{sinc}[T_p(f + \gamma t_{\text{tor}})] \cdot \exp[-i2\pi(f + \gamma t_{\text{tor}})t_{\text{tor}} - i2\pi f_c t_{\text{tor}}] \quad (26)$$

which is independent of  $t_{\text{ref}}$  and which has a phase  $(-2\pi f_c t_{\text{tor}})$  proportional to  $t_{\text{tor}} = 2R/c$  at  $f'_s = -\gamma t_{\text{tor}}$ . The time-domain counterpart of (26) is

$$s'_{\text{IF}}(\hat{t}) = A \cdot P \left( \frac{\hat{t} - t_{\text{tor}}}{T_p} \right) \cdot \exp[-i2\pi(f_c + \gamma \hat{t})t_{\text{tor}}]. \quad (27)$$

It follows that an additional processing step is needed that transforms  $S_{\text{IF}}(f)$  in (25) into  $S'_{\text{IF}}(f)$  in (26), namely,

$$S'_{\text{IF}}(f) = S_{\text{IF}}(f + \gamma t_{\text{ref}}) \cdot \exp[-i2\pi f_c t_{\text{ref}} - i2\pi\gamma t_{\text{ref}} \Delta t - i\pi\gamma(\Delta t)^2]. \quad (28)$$

This processing step eliminates the dependence on the chosen reference point as well as the second-order range and phase-delays,  $2\pi\gamma t_{\text{ref}} \Delta t$  and  $\pi\gamma(\Delta t)^2$ .

However, we note that the implementation of the processing step in (28) is in principle not possible because  $\Delta t = t_{\text{tor}} - t_{\text{ref}}$  is itself dependent on the distance to the scattering center through  $t_{\text{tor}}$  and is thus unknown. It becomes possible only if the two exponential terms depending on  $\Delta t$  satisfy the approximations

$$\exp[-i\pi\gamma(\Delta t)^2] \approx 1 \quad (29)$$

$$\exp(-i2\pi\gamma t_{\text{ref}} \Delta t) \approx 1. \quad (30)$$

If (29) and (30) are satisfied, the processing step in (28) is implemented as

$$S'_{\text{IF}}(f) \approx S_{\text{IF}}(f + \gamma t_{\text{ref}}) \cdot \exp(-i2\pi f_c t_{\text{ref}}). \quad (31)$$

As an example, our prototype is designed with a frequency bandwidth  $B = 5.8$  GHz and sweeping time  $T_p = 20 \mu\text{s}$ ; thus,  $\gamma = B/T_p = 2.9 \cdot 10^{14}$  Hz/s. The inspected person is expected to stand at about  $R_{\text{ref}} \approx 0.4$  m from the transceiver array, in which case  $t_{\text{ref}} = 2R_{\text{ref}}/c \approx 2.7 \cdot 10^{-9}$  s. At the same time, the target's extent from the reference position in any given direction satisfies  $\Delta R < 0.5$  m; see (22). In fact, at a stand-off distance of about 0.4 m,  $\Delta R$  is further reduced due to the limited beamwidth of the antennas (about 60°). This means that the exponents' arguments in (29) and (30) satisfy  $\pi\gamma(\Delta t)^2 < 0.01$  and  $2\pi\gamma t_{\text{ref}} \Delta t < 0.02$  thereby ensuring that the approximations (29) and (30) are sufficiently accurate (relative error less than 2%).

As we show later, violating (29) and (30) leads to unfocused images, the errors of which grow with the errors in the approximation. For a given frequency modulation slope  $\gamma$ , the approximations dictate limitations on  $R_{\text{ref}}$  and  $\Delta R_{\text{max}}$ , where  $\Delta R_{\text{max}}$  is the maximum difference between the distances from transceiver to the reference point and that to a target point. The respective max phases in the exponents in (29) and (30) are

$$\phi_{1\text{max}} = \pi\gamma(\Delta t)_{\text{max}}^2 = (4\pi\gamma/c^2)\Delta R_{\text{max}}^2 \quad (32)$$

$$\phi_{2\text{max}} = 2\pi\gamma t_{\text{ref}} \Delta t_{\text{max}} = (8\pi\gamma/c^2)R_{\text{ref}}\Delta R_{\text{max}}. \quad (33)$$

In order the relative errors in the approximations to be less than 5%,  $\phi_{1\text{max}}$  and  $\phi_{2\text{max}}$  must not exceed 2.5°.

*4) Inversion:* The echo signal of the target can be viewed as the superposition of the echo signals of all scattering points within the imaged domain. According to (14), (15), and (27), this cumulative signal is

$$s'_{r,\text{IF}}(\mathbf{r}_r, \hat{t}) = \iiint \sigma(\mathbf{r}_o) P \left( \frac{\hat{t} - 2R(\mathbf{r}_o)/c}{T_p} \right) \cdot \frac{\exp[-i2\pi(f_c + \gamma \hat{t})2R(\mathbf{r}_o)/c]}{R(\mathbf{r}_o)} d\mathbf{r}_o. \quad (34)$$

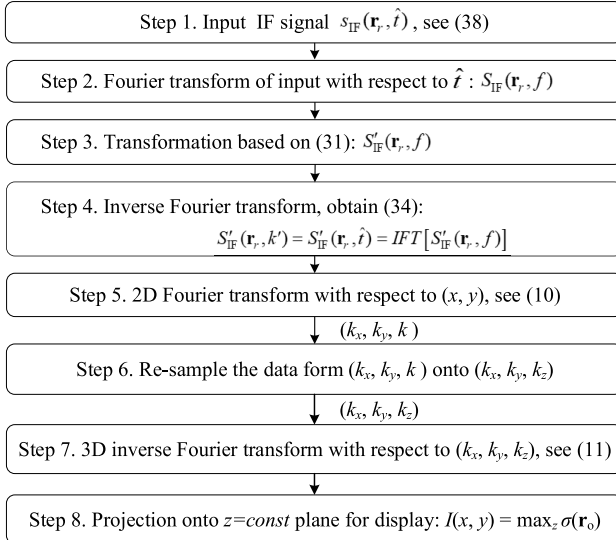


Fig. 2. Flowchart of the GHI-LFM inversion algorithm.

We can define an equivalent time-dependent frequency and wave number as

$$f' = f_c + \gamma \hat{t}, \quad k' = 2\pi f'/c. \quad (35)$$

Then, (34) can be written as

$$s'_{r,IF}(\mathbf{r}_r, k') = \iiint \sigma(\mathbf{r}_o) [\exp(-i2k'R)/R] d\mathbf{r}_o \quad (36)$$

provided that

$$-\frac{T_p}{2} + \frac{2R}{c} \leq \hat{t} \leq \frac{T_p}{2} + \frac{2R}{c}. \quad (37)$$

The comparison of (4) and (36) reveals that the inversion procedure in described in Section II-A, see (11), can be used directly to retrieve  $\sigma(\mathbf{r}_o)$ .

The development from (23) to (36) provides the general theory of the holographic reconstruction with LFM radar. Importantly, it shows that the holographic reconstruction formulas used with frequency-stepped signals can be applied directly to the down-converted LFM signals only if the approximations in (29) and (30) hold.

*5) GHI-LFM Algorithm:* The input to the inversion algorithm is the received IF signal, which, according to (14) and (23), is

$$\begin{aligned} s_{IF}(\mathbf{r}_r, \hat{t}) = & \iiint \frac{\sigma(\mathbf{r}_o)}{R(\mathbf{r}_o)} \cdot P\left(\frac{\hat{t} - t_{\text{tor}}}{T_p}\right) \cdot \exp(-i2\pi f_c \Delta t) \\ & \cdot \exp[-i2\pi \gamma (\hat{t} - t_{\text{ref}}) \Delta t] \cdot \exp[i\pi \gamma (\Delta t)^2] \cdot d\mathbf{r}_o. \end{aligned} \quad (38)$$

Its processing is summarized in the flowchart in Fig. 2.

### III. PERFORMANCE ANALYSIS WITH SYNTHETIC DATA

The GHI-LFM algorithm's performance analysis includes metrics based on the image PSF and a benchmark target. Spatial resolution limits and robustness to system errors and additive noise are assessed quantitatively using objective metrics [62], [63].

TABLE I  
SIMULATION PARAMETERS USED IN THE SYNTHETIC EXAMPLE

Parameters	Value
Center frequency ( $f_c$ )	29.9 GHz
Frequency bandwidth ( $B$ )	5.8 GHz
Sampled frequency points	200
Frequency sweeping time	20 $\mu$ s
Target pixel size along X	0.5 mm
Number of pixels along X	1200
Target pixel size along Y	0.5 mm
Number of pixels along Y	1200
Aperture samples along X	120
Aperture sampling interval along X	5 mm
Aperture samples along Y	120
Aperture sampling interval along Y	5 mm

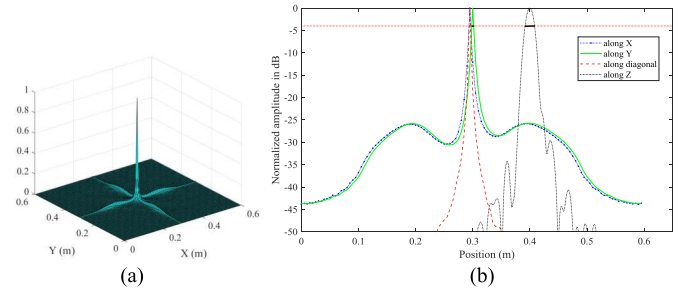


Fig. 3. (a) Illustration of the IPSF projected along range. (b) Cut lines through the IPSF along  $x$ ,  $y$ ,  $z$ , and the cross-range diagonal.

The results in this section are all based on synthetic data—the IF echo signals simulated by (38). The system parameters used to generate the synthetic data are listed in Table I.

#### A. Point Spread Function

The image PSF (IPSF) provides basic means to compare imaging algorithms [64]–[68]. The GHI-LFM IPSF is obtained here for a point scatterer at 0.4 m from the transceiver plane. Its lateral position is  $x = 0.3$  m and  $y = 0.3$  m. The point scatterer is infinitesimal in theory whereas in simulations and measurements it must be electrically very small. Here, its size is set equal to a pixel of 0.5 mm (the minimum wavelength is  $\lambda_{\min} = 9.14$  mm). Fig. 3(a) shows the IPSF after projecting the 3-D image onto a  $z = \text{const}$  plane (see Step 8 in the algorithm flowchart in Fig. 2). The IPSF width at  $-4$  dB indicates the spatial resolution in the respective direction [47]. Fig. 3(b) shows the line cuts of the projected IPSF along  $x$ ,  $y$ , and the diagonal at  $45^\circ$  relative to  $x$ . It also shows the line cut of the 3-D IPSF along  $z$ . The results indicate resolution limits of: 4.8 mm along  $x$ , 4.9 mm along  $y$ , 4.2 mm along the cross-range diagonal, and 16.5 mm along range. The side-lobe levels are below  $-25$  dB in all directions. They are the lowest close to the cross-range diagonal. The resolution limits above are consistent with the theoretical limits of  $\lambda_{\min}/2 \approx 4.6$  mm along cross-range and  $c/(2B) \approx 25.8$  mm along range.

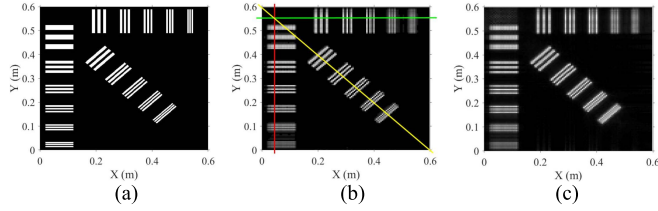


Fig. 4. Benchmark target. (a) True image. (b) Reconstructed 3-D image at slice  $z = 0.4$  m, with the three line cuts along which the 1-D plots in Figs. 5–7 are generated. (c) Projected 2-D reconstruction along range.

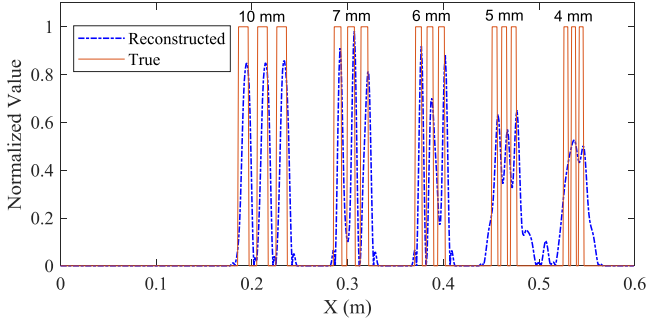


Fig. 5. True and reconstructed target profiles in the horizontal ( $X$ ) direction.

### B. Spatial Resolution Evaluation With Benchmark Target

To validate the spatial resolution with complex targets, various standard benchmark structures have been proposed [69], [70]. We have designed the benchmark target shown in Fig. 4(a), which consists of sets of perfectly conducting strips in air. It allows for determining the combined impact of the size of each scattering object (a conducting strip) and the proximity to other objects. Three groups of metal strips have distinct orientations: horizontal, vertical, and diagonal. Within each group, the width and separation distances of the strips vary.

The benchmark target is placed 0.4 m from the transceiver array. All strips are 100 mm long. The horizontal group includes five sets of vertical strips. The space between any two neighboring sets is 50 mm. From left to right, the strip widths within each set are: 10, 7, 6, 5, and 4 mm. In each set, the gap between any two adjacent strips is the same as the strip width. The diagonal group is a rotated (45° clockwise) duplicate of the horizontal one. The vertical group involves an additional set of 20-mm-wide strips with a gap of 20 mm.

The slice of the 3-D GHI-LFM reconstruction at  $z = 0.4$  m is shown in Fig. 4(b). The figure also shows the lines along which image cuts are taken to estimate quantitatively the cross-range spatial resolution in the horizontal, vertical and diagonal directions. The projected 2-D image is also shown; see Fig. 4(c). The horizontal line cut through the image in Fig. 4(b) is shown in Fig. 5 (dash line) along with the true reflectivity (solid line). The analogous plots of the diagonal and vertical line cuts are shown in Figs. 6 and 7, respectively.

In Fig. 5, we observe that the sets with strip widths from 5 to 10 mm are identified well. The strip set with 4 mm width shows only two peaks where there should be three. Thus, the horizontal spatial resolution limit is about 5 mm. Fig. 6 indicates that the diagonal resolution is about 4 mm since the strips at this width and separation are well differentiated.

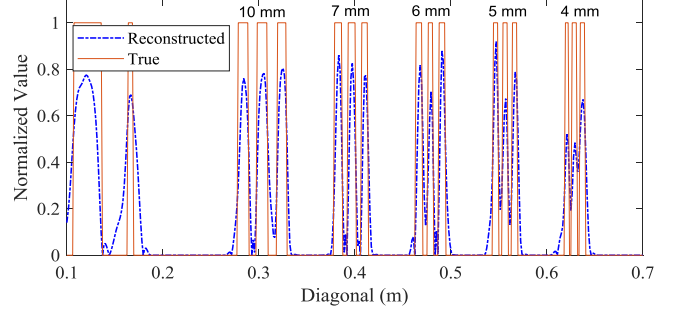


Fig. 6. True and reconstructed target profiles in the diagonal direction.

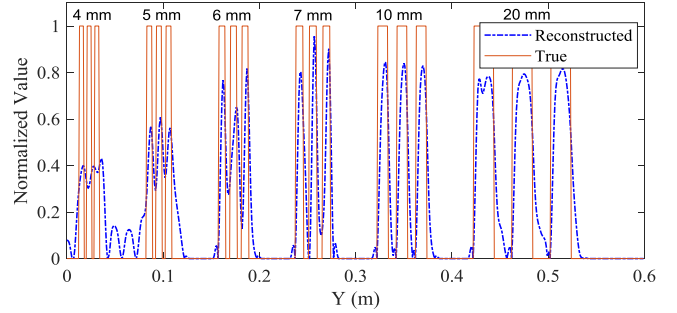


Fig. 7. True and reconstructed target profiles in the vertical ( $Y$ ) direction.

Fig. 7 shows that the vertical resolution limit is very similar to the horizontal one. All these results are consistent with the resolution limits indicated by the IPSF (see Section III-A).

### C. Comparison With the Previous Holographic Formula

The proposed GHI-LFM algorithm utilizes the inversion formula (11) in the last stage of the LFM signal processing. As indicated in Section II-A, this formula differs from the classical holographic formula [13] by its ability to account for the magnitude decay associated with the spherical spread of the backscattering. Since this decay impacts the field distribution more significantly in close-range measurements, it is desirable to compare the output of the two inversion formulas for targets at various stand-off distances. For a fair comparison, the same steps in the signal-processing chain are followed as in Fig. 2 in both cases. The difference is only in Step 7, where we use either our inversion formula (11) or the classic one [13].

To quantify the comparison, the root mean square error (RMSE) between the reconstructed reflectivity  $\sigma_r$  and the true one  $\sigma_o$  is used. It is defined as

$$\text{RMSE} = \sqrt{\frac{1}{MN} \sum_{m=1}^M \sum_{n=1}^N [\sigma_r(n, m) - \sigma_o(n, m)]^2} \quad (39)$$

where  $\sigma_r(n, m)$  and  $\sigma_o(n, m)$  are the respective pixel values at the grid point  $(n, m)$  in the image of size  $N \times M$ . In the case of the true target,  $\sigma_o = 1$  at points belonging to metallic strips and  $\sigma_o = 0$  otherwise. In the reconstructed image,  $\sigma_r$  can assume values between 0 and 1. Another metric for the image quality is the structural similarity (SSIM) index as defined in [71]. SSIM assumes values between 0 and 1. Larger SSIM means better agreement between the reconstructed and the actual targets.

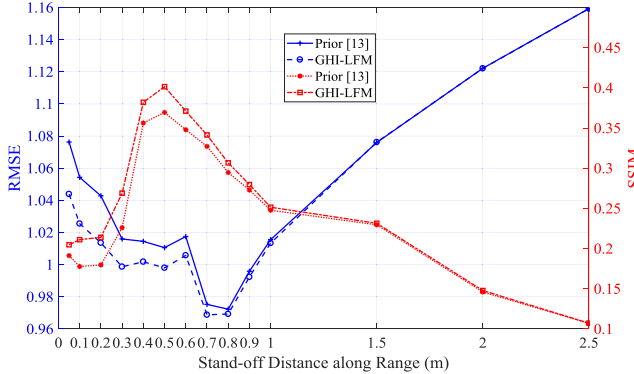


Fig. 8. Comparison of prior method and GHI-LFM algorithm.

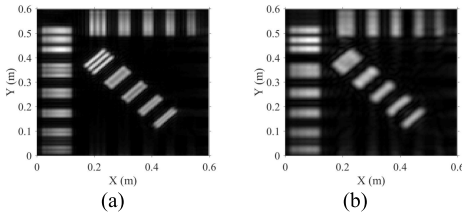


Fig. 9. Reconstructed images of the benchmark target at a stand-off distance. (a) 1.5 m. (b) 2.5 m. The images are unfocused due to the violation of the approximations (29) and (30).

The data with the synthetic benchmark target in Fig. 4(a) are acquired at different stand-off distances  $d$  from the transceiver array. In the reconstruction, the reference distance is always set as  $R_{\text{ref}} = d$ , i.e., the reference point is at the center of the target's plane, which, in turn is at a distance  $d$  from the acquisition plane. The system parameters are the ones listed in Table I. The comparison of the two inversion formulas through RMSE and SSIM is presented in Fig. 8. It is evident that the proposed inversion formula (11) performs better than the classic formula, especially at smaller stand-off distances (below 1 m). At larger stand-off distances, the image errors for both inversion formulas tend to be similar and grow with distance, which is due to the violation of the approximations (29) and (30) as discussed next.

#### D. Limitations of Holography With LFM Signals

The LFM radar prototype has been designed for imaging ranges below 1 m, dictating the choice of the frequency modulation slope  $\gamma$  (see Table I). When the stand-off distance  $d = R_{\text{ref}}$  exceeds 1 m, the approximations (29) and (30) may no longer hold. Typically, the object zone is assumed to extend along range from  $d - R_{\text{ref}}/2$  to  $d + R_{\text{ref}}/2$ . If, for example,  $d = 1.5$  m, then  $\Delta R_{\text{max}} \approx 0.8$  m, which leads to  $\phi_1 \approx 0.025$  and  $\phi_2 \approx 0.096$ ; see (32) and (33). Accordingly, the errors in the approximations (29) and (30) are 2.53% and 9.59%, respectively. The second error exceeds 5% considerably, leading to unacceptable image quality as shown in Fig. 9(a). Fig. 9(b) shows the image of the benchmark target at a stand-off distance of 2.5 m, where the errors in the approximations (29) and (30) are even larger.

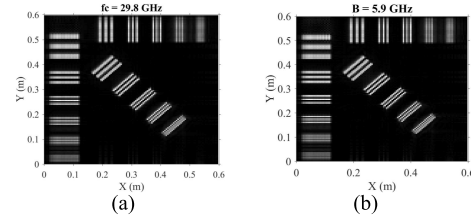


Fig. 10. Reconstructed images of the benchmark target when the data have system frequency errors. (a) Center frequency is 29.8 GHz instead of 29.9 GHz. (b) Frequency bandwidth is 5.9 GHz instead of 5.8 GHz. The reconstruction algorithm assumes center frequency of 29.9 GHz and bandwidth of 5.8 GHz.

#### E. Algorithm Tolerance to Frequency Errors

Advanced manufacturing technologies have made the millimeter-wave radar technology precise and stable. Nonetheless, the performance of the reconstruction algorithm needs to be verified with regard to the frequency errors. In a well-designed LFM millimeter-wave radar, these errors stem from the FM linearity (the ratio of maximum frequency error to bandwidth [72]), which should not exceed 0.5%. Thus, in the current prototype, the frequency error from 27 to 32.8 GHz is limited within 30 MHz.

To verify the algorithm's tolerance to frequency errors, we have introduced intentional errors in the synthetic data with the benchmark target. Two separate types of tests are carried out: 1) error in the central frequency (bandwidth kept at 5.8 GHz) and 2) error in the bandwidth (central frequency kept at 29.9 GHz). The reconstruction algorithm, on the contrary, always assumes a central frequency of 29.9 GHz and bandwidth of 5.8 GHz. Two sample images are shown in Fig. 10. Fig. 10(a) shows the reconstructed image when the central frequency of the scattered data is 100 MHz lower than the expected 29.9 GHz. Fig. 10(b) shows the image when the bandwidth of the scattered data is 100 MHz wider than the expected 5.8 GHz. Both of these images are visibly identical to the one in Fig. 4(b), where the data has not been intentionally corrupted. For the image in Fig. 4(b), the RMSE and SSIM are 1.0070 and 0.3820, respectively. For the image in Fig. 10(a), these values are 1.008 and 0.3807, whereas for the image in Fig. 10(b), they are 1.0140 and 0.3712. This represents less than 5% deterioration in the RMSE and the SSIM compared to the ideal scenario, which indicates no deterioration of the image quality. We conclude that the GHI-LFM algorithm has high tolerance to frequency errors in the imaging systems.

#### F. Noise Studies With Synthetic Benchmark Data

To study the method's robustness to noise, additive white Gaussian noise is introduced into the simulated echo data. The white Gaussian noise is added using the MATLAB function `awgn(X, SNR, "measured")` [73], where  $X$  denotes the data, SNR is the signal-noise ratio in dB, and "measured" instructs the function to compute the data signal power before adding noise. Some representative reconstructed images are shown in Fig. 11. The RMSE and SSIM values at different noise levels are reported in Table II. We observe that when the SNR decreases to 2 dB, the RMSE increases to 1.0567 but is still below the 5% threshold of RMSE deterioration.

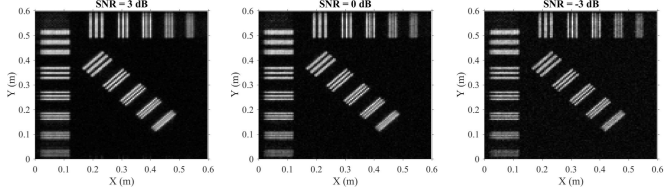


Fig. 11. Results with different SNR levels.

TABLE II  
RMSE AND SSIM AT VARIOUS ADDITIVE NOISE LEVELS

SNR (dB)	RMSE	SSIM
Ideal	1.0069	0.38204
21	1.0071	0.36351
20	1.0071	0.35845
10	1.0098	0.23907
3	1.0392	0.12846
2	1.0567	0.12367
0	1.0797	0.09666
-3	1.1603	0.07207
-7	1.3759	0.05146



Fig. 12. Photograph of imaging prototype.

However, the SSIM decreases sharply with the SNR, reaching a value of 0.12367 at SNR = 2 dB. This value exceeds the 5% deterioration-threshold for SSIM (about 0.3629). Only when  $\text{SNR} > 20 \text{ dB}$ , SSIM is within the 5% deterioration-threshold of the ideal case in Fig. 4(b). It appears that the image SSIM is far more sensitive to the noise levels than the RMSE.

However, Fig. 11 shows the images corresponding to SNR of 3, 0, and  $-3 \text{ dB}$ . It is evident that even with  $\text{SNR} = -3 \text{ dB}$ , the benchmark targets are well identified although the rise in the image noise in the target-free regions is also appreciable.

#### IV. IN-HOUSE PROTOTYPE AND SYSTEM CALIBRATION

The GHI-LFM algorithm is implemented with an in-house 3-D millimeter-wave imaging prototype. A photo of the planar scanner is shown in Fig. 12 [58]. It utilizes a linear array of antennas (see horizontal bar in Fig. 12), which is scanned mechanically in the vertical direction to quickly gather the echo data in about 2 s. The antenna array is driven by a wide-band millimeter-wave transceiver, which transmits LFM signals and demodulates the echo signals to baseband through de-chirping; see (17). During the vertical scan, the antennas in the horizontal array are sequentially switched at a very high

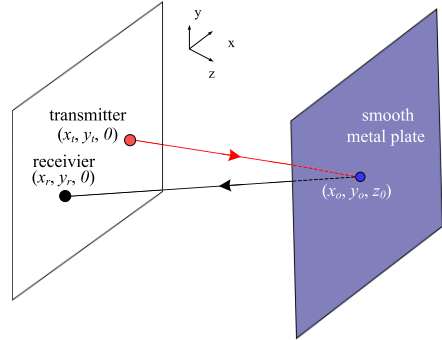


Fig. 13. Schematic of a system calibration measurement.

speed (about  $30 \mu\text{s}$  per channel) to gather the data in each row of the sampling grid, thereby providing a full data set over a 2-D aperture.

During vertical mechanical scanning, horizontal electronic scanning, and broadband frequency scanning, the measurement is susceptible to various types of uncertainties. The echo signal is down-converted to obtain  $I$  and  $Q$  IF signal components. Due to the slight asymmetry of the demodulator circuit, the imperfections of the devices in each branch ( $I$  and  $Q$ ), and the slight instantaneous frequency changes with the ambient temperature, the amplitude, and phase characteristics of  $I$  and  $Q$  branches may be unbalanced. Additionally, the amplitudes and phases among all signals received through the multiplexed RF channels may also be inconsistent due to manufacturing tolerances in the antenna arrays and the RF switch networks. Calibration is therefore absolutely necessary.

We use a simple but effective calibration scheme, which is depicted in Fig. 13. The calibration employs a flat  $1 \text{ m} \times 1 \text{ m}$  metallic plate serving as an ideal reflector, represented by its scattering coefficient  $\sigma(\mathbf{r}_o)$ . While calibrating, the Rx antenna is assumed to be at a known fixed plane ( $x, y, z = 0$ ). The metallic plate is fixed at  $z_o = \text{const}$  and assumed to have a reference scattering coefficient  $\sigma(x_o, y_o) = 1$  (ignoring the phase reversal). As per (34), the echo data due to the metallic plate is

$$s(x, y, \hat{t}) = \iint_{S_M} \frac{1}{R} P \left( \frac{\hat{t} - 2R/c}{T_p} \right) \exp \left[ -i \frac{4\pi R}{c} (f_c + \gamma \hat{t}) \right] dx_o y_o \quad (40)$$

where  $S_M$  is surface of the metallic plate.

Assume that the actual echo data received by a channel is  $s_m(\hat{t})$ , represented by its  $I$  and  $Q$  components. The respective theoretical echo data obtained with (40) is  $s_t(\hat{t})$ . The amplitude calibration coefficient for this channel is calculated as the ratio of the peak signal strengths  $A_{tp} = \max\{|s_t(\hat{t})|\}$  and  $A_{tm} = \max\{|s_m(\hat{t})|\}$ , i.e.,  $m_{\text{cal}} = A_{tp}/A_{tm}$ . The time-dependent phases  $\varphi_t(\hat{t})$  and  $\varphi_m(\hat{t})$  of  $s_t(\hat{t})$  and  $s_m(\hat{t})$ , respectively, are subtracted to obtain the phase correction  $\varphi_{\text{cal}}(\hat{t}) = \varphi_t(\hat{t}) - \varphi_m(\hat{t})$ . Finally, a correction is applied to every channel during actual measurement using

$$s_{\text{cal}}(\hat{t}) = m_{\text{cal}} s_m(\hat{t}) \cdot \exp(i \varphi_{\text{cal}}). \quad (41)$$

The calibrated signals are the input to the GHI-LFM algorithm.

TABLE III

SYSTEM PARAMETERS IN THE IMAGING EXPERIMENTS WITH THE IN-HOUSE MILLIMETER-WAVE LFM SYSTEM

Parameters	Value
Center frequency	29.9 GHz
Frequency bandwidth	5.8 GHz
Sampled frequency points	200
Sweeping time	20 $\mu$ s
Array element number	80 pairs
Array length	80 cm
Scan height	190 cm
Aperture samples along X	159
Aperture sampling interval along X	5 mm
Aperture samples along Y	379
Aperture sampling interval along Y	5 mm

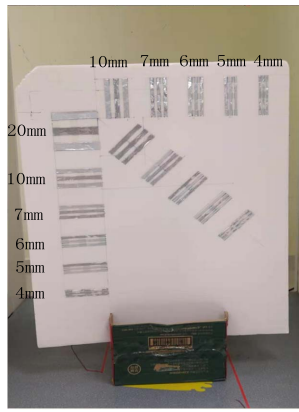


Fig. 14. Fabricated benchmark target.

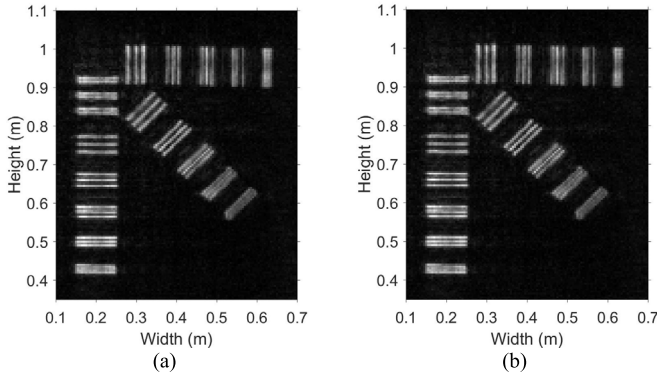


Fig. 15. (a) Reconstructed result using the GHI-LFM algorithm. (b) Reconstructed result using the classic method [13].

## V. EXPERIMENTAL VALIDATION

The system parameters are listed in Table III. Consistent with the benchmark target used in the synthetic validation example of Section III, a benchmark target has been fabricated (shown in Fig. 14) using adhesive tinfoil strips glued to a *Styrofoam* panel. It is placed about 0.4 m from the scanning array. The reconstructed image of the target produced by the GHI-LFM algorithm is shown in Fig. 15(a), and that by the classic approach (see [13]) is shown in Fig. 15(b). It is difficult to distinguish the imaging qualities of the two images, because the SSIM value of them is 0.9961, very close to 1.

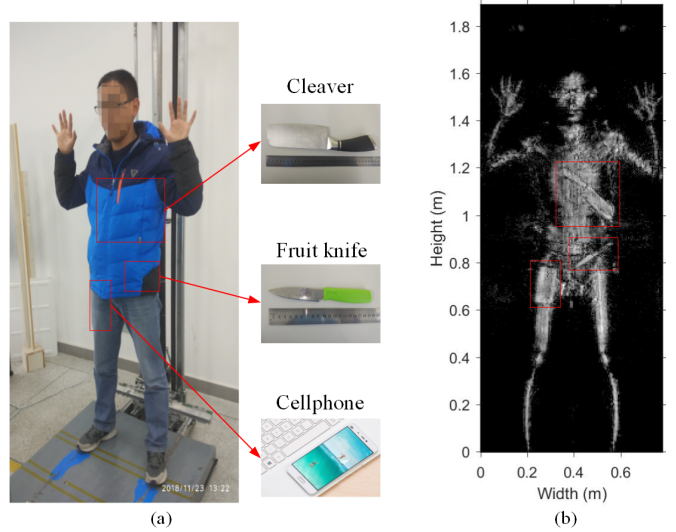


Fig. 16. (a) Scene with a volunteer undergoing a security check. (b) Reconstructed image showing objects (cleaver, fruit knife, and cellphone) concealed under the jacket (marked with red rectangles).

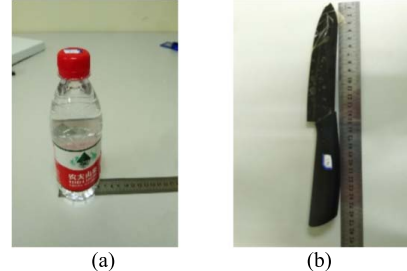


Fig. 17. Objects used to test the detection capability of the imaging prototype with nonmetallic hidden items. (a) Bottled water. (b) Ceramic knife.

It is evident from Fig. 15 that the strip sets with width larger than 5 mm have been clearly identified in the vertical and oblique groups. In the horizontal group, only strips of width equal to or greater than 6 mm can be clearly recognized. It is evident that the spatial resolution of the experimental system is somewhat worse than the resolution limits obtained with synthetic data in Section III-A. This is expected in view of the presence of noise and background reflections.

The careful inspection of Fig. 15 indicates that the reconstruction quality varies with the strip orientation. For the set with the same strip width, the resolution of the reconstructed result in the vertical group is better than that of the horizontal group. This is due to: 1) the aperture size being larger in the vertical direction than in the horizontal direction and 2) the linear polarization of the antennas.

The system integrating the GHI-LFM algorithm is also tested with an actual scan of a volunteer; see Fig. 16(a). The volunteer stands at about 0.4 m away from the scanning array with a thick down jacket and a hidden metallic cleaver (55 mm in width, about 1 mm thick) and fruit knife (20 mm in width, about 0.5 mm thick) under it. There is a mobile phone in the side pocket. The reconstructed image is shown in Fig. 16(b), which clearly shows the shapes of cleaver, knife, and cellphone.

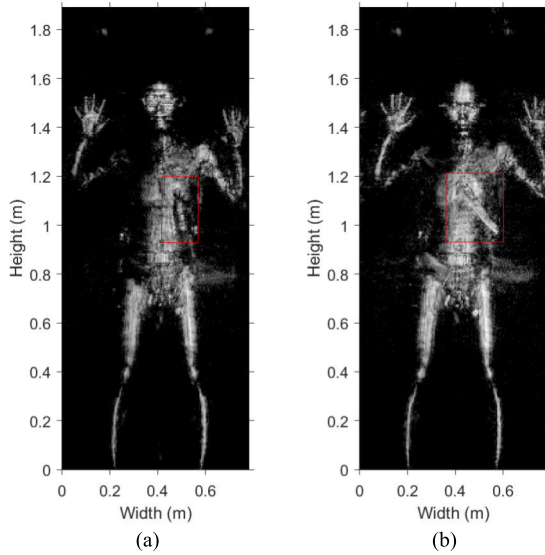


Fig. 18. MMW images of a volunteer wearing a down jacket with (a) bottled water and (b) ceramic knife.

The ability of millimeter-wave imaging systems to detect metallic objects is well documented, see [13], [15], [32], [37], [51]. However, the case of nonmetallic objects can be challenging. We have tested the system with various emulated contraband samples with different textures. Here, we show two representative results. Fig. 17 shows two of the objects used as hidden items: bottled water (60 mm in diameter and 180 mm in height) and ceramic knife (30 mm in width, about 1 mm thick). The objects are hidden under a thick down jacket on a person, one at a time, measured and imaged by GHI-LFM. The respective MMW images are shown in Fig. 18. The images, although less clear than those with metallic objects, are sufficiently good to detect the nonmetallic objects. Note that in both images, we can see a coin in the person's pocket (upper portion of thigh on the right). Even the facial expressions of the volunteer can be recognized to some extent. We also observe that the middle part of the bottled water is brighter than its edges, which is due to the differences in the direction of scattering. The reflectivity of the ceramic knife, while smaller than that of a metallic knife, is sufficient to exceed the reflectivity of the human body.

## VI. CONCLUSION

A holographic inversion algorithm, GHI-LFM, is proposed for image reconstruction with LFM radars and is applied to the millimeter-wave security screening of people. The algorithm is based on a general theory of the holographic image reconstruction with LFM signals. The method offers an improved holographic inversion formula and presents a rigorous mathematical model explicitly stating how the LFM radar parameters (the frequency-modulation slope  $\gamma$ ) determine the limitation of the imaging system in terms of object zone and its distance from the radar; see (29) and (30).

Through synthetic examples with simulated data and actual experiments with an in-house prototype, it is shown that the GHI-LFM method is robust against noise and uncertainty in the system parameters such as frequency errors. The GHI-LFM is highly tolerant to central-frequency deviations as well as

uncertainties in the frequency-modulation slope  $\gamma$  (or equivalently, the frequency bandwidth  $B$ ). With additive white Gaussian noise, a high-quality image of the benchmark object is obtained even with SNR of 2 dB, judging only by RMSE.

With LFM from 27 to 32.8 GHz, the spatial resolution limit of the GHI-LFM algorithm is estimated to be about 5 mm based on both simulated and experimental data. These results agree with the theoretical limit of about half-wavelength.

Further, a simple calibration approach is utilized based on a measurement with a metallic plate, which ensures that system uncertainties and fabrication tolerances are effectively de-embedded from the measured signals.

An in-house prototype implements fast 2-D planar scanning (less than 2 s) and generates the GHI-LFM images in less than 1 s. The reconstruction algorithm has been tested with volunteers carrying various objects under a thick jacket, both metallic (knives and cleaver) and nonmetallic (bottled water, ceramic knife). The tests demonstrate that all objects can be clearly detected in the images. Numerous other experiments have been carried out (not shown for brevity) investigating the effect of fabrics blocking concealed items: shirt, down jacket, sweater, and wool coat. Slight image deterioration has been observed only with the wool coat, which seems to introduce signal attenuation sufficient to reduce the SNR.

## REFERENCES

- [1] *Guide to the Technologies of Concealed Weapon and Contraband Imaging and Detection*, U.S. Department of Justice, Office of Justice Programs, National Institute of Justice, Washington, DC, USA, 2001. [Online]. Available: <https://www.ncjrs.gov/pdffiles1/nij/184432.pdf>
- [2] D. J. Daniels, *EM Detection of Concealed Targets*. Hoboken, NJ, USA: Wiley, 2010.
- [3] B. Y. Kapilevich, S. W. Harmer, and N. J. Bowring, *Non-Imaging Microwave and Millimetre-Wave Sensors for Concealed Object Detection*. Boca Raton, FL, USA: CRC Press, 2017.
- [4] *Walk-Through Metal Detectors for Use in Concealed Weapon and Contraband Detection*, U.S. Department of Justice, Office of Justice Programs, National Institute of Justice, Washington, DC, USA, 2003. [Online]. Available: <https://www.ncjrs.gov/pdffiles1/nij/193510.pdf>
- [5] N. K. Nikolova and J. J. McCombe, “On-body concealed weapon detection system,” U.S. Patent 10229328, Mar. 12, 2019. [Online]. Available: <https://patentimages.storage.googleapis.com/0fd51e/a1a32e2f905ec5/US20150379356A1.pdf>
- [6] A. Agurto, Y. Li, G. Y. Tian, N. Bowring, and S. Lockwood, “A review of concealed weapon detection and research in perspective,” in *Proc. IEEE Int. Conf. Netw., Sens. Control*, London, U.K., Apr. 2007, pp. 443–448.
- [7] P. W. Kruse and D. D. Skatrud, *Uncooled Infrared Imaging Arrays and Systems*. San Diego, CA, USA: Academic Press, 1997.
- [8] R. Appleby and H. B. Wallace, “Standoff detection of weapons and contraband in the 100 GHz to 1 THz region,” *IEEE Trans. Antennas Propag.*, vol. 55, no. 11, pp. 2944–2956, Nov. 2007.
- [9] D. M. Sheen, A. M. Jones, and T. E. Hall, “Simulation of active cylindrical and planar millimeter-wave imaging systems,” *Proc. SPIE*, vol. 10643, May 2018, Art. no. 1063408.
- [10] Q. Ma, H. Chung, and G. M. Rebeiz, “A 4-channel 10–40 GHz wideband receiver with integrated frequency quadrupler for high resolution millimeter-wave imaging systems,” in *IEEE MTT-S Int. Microw. Symp. Dig.*, Philadelphia, PA, USA, Jun. 2018, pp. 883–886.
- [11] S. Li, G. Zhao, H. Sun, and M. Amin, “Compressive sensing imaging of 3-D object by a holographic algorithm,” *IEEE Trans. Antennas Propag.*, vol. 66, no. 12, pp. 7295–7304, Dec. 2018.
- [12] D. M. Sheen, D. L. McMakin, H. D. Collins, T. E. Hall, and R. H. Severtsen, “Concealed explosive detection on personnel using a wideband holographic millimeter-wave imaging system,” *Proc. SPIE*, vol. 2775, pp. 503–512, Jun. 1996.
- [13] D. M. Sheen, D. L. McMakin, and T. E. Hall, “Three-dimensional millimeter-wave imaging for concealed weapon detection,” *IEEE Trans. Microw. Theory Techn.*, vol. 49, no. 9, pp. 1581–1592, Sep. 2001.

- [14] D. Sheen, D. McMakin, and T. Hall, "Near-field three-dimensional radar imaging techniques and applications," *Appl. Opt.*, vol. 49, no. 19, p. E83–E93, 2010.
- [15] S. S. Ahmed, A. Schiessl, and L.-P. Schmidt, "A novel fully electronic active real-time imager based on a planar multistatic sparse array," *IEEE Trans. Microw. Theory Techn.*, vol. 59, no. 12, pp. 3567–3576, Dec. 2011.
- [16] ProVision2, *L3HARRIS Security & Detection Systems*. Accessed: Dec. 27, 2019. [Online]. Available: <https://www.sds.l3t.com/advanced-imaging/provision-2.htm>
- [17] ProVision AT, *L3HARRIS Security & Detection Systems*. Accessed: Dec. 27, 2019. [Online]. Available: <https://www.sds.l3t.com/advanced-imaging/provision-at.htm>
- [18] SafeView, *L3HARRIS Security & Detection Systems*. Accessed: Dec. 27, 2019. [Online]. Available: <https://www.sds.l3t.com/advanced-imaging/safeview.htm>
- [19] Rohde & Schwarz R&S QPS Quick Personnel Security Scanner. Accessed: Dec. 27, 2019. [Online]. Available: [https://cdn.rohde-schwarz.com/us/campaigns\\_2/a\\_d/qps\\_2/QPS\\_Fact-Sheet.pdf](https://cdn.rohde-schwarz.com/us/campaigns_2/a_d/qps_2/QPS_Fact-Sheet.pdf)
- [20] EQO, *Smiths Detection*. Accessed: Dec. 27, 2019. [Online]. Available: <https://www.smithsdetection.com/products/eqo/>
- [21] D. Gabor, "A new microscopic principle," *Nature*, vol. 161, no. 4098, pp. 777–778, May 1948.
- [22] E. N. Leith and J. Upatnieks, "Reconstructed wavefronts and communication theory," *J. Opt. Soc. Amer.*, vol. 52, no. 10, pp. 1123–1130, 1962.
- [23] R. K. Mueller, "Acoustic holography," *Proc. IEEE*, vol. 59, no. 9, pp. 1319–1335, Sep. 1971.
- [24] G. Tricoles and N. H. Farhat, "Microwave holography: Applications and techniques," *Proc. IEEE*, vol. 65, no. 1, pp. 108–121, Jan. 1977.
- [25] N. H. Farhat and W. R. Guard, "Millimeter wave holographic imaging of concealed weapons," *Proc. IEEE*, vol. 59, no. 9, pp. 1383–1384, Sep. 1971.
- [26] G. Zhu, Z. Dong, and D. Liang, "BP imaging algorithm of Ultra-wideband LFM signal," *Signal Process.*, vol. 17, no. 5, pp. 424–428, 2001.
- [27] H. Yu, Y. Zhang, and L. Zhu, "UWB LFMCW radar imaging based on dechirp processing," *Mod. Radar*, vol. 27, no. 7, pp. 39–41, 2005.
- [28] A. F. Yegulalp, "Fast backprojection algorithm for synthetic aperture radar," in *Proc. IEEE Radar Conf. Radar into Next Millennium*, Waltham, MA, USA, Apr. 1999, pp. 60–65.
- [29] M. I. Duersch, "Backprojection for synthetic aperture radar," Ph.D. dissertation, Dept. Elect. Comput. Eng., Brigham Young Univ., Provo, UT, USA, 2013.
- [30] M. Kazemi, Z. Kavehvash, and M. Shabany, "K-space aware multi-static millimeter-wave imaging," *IEEE Trans. Image Process.*, vol. 28, no. 7, pp. 3613–3623, Jul. 2019.
- [31] A. Gaibel and A. Boag, "Back-projection SAR imaging using FFT," in *Proc. Eur. Radar Conf. (EuRAD)*, London, U.K., Oct. 2016, pp. 69–72.
- [32] Z. Briqech, S. Gupta, A. A. Beltayib, A. Elboushi, A-R. Sebak, and T. A. Denidni, "57-64 GHz imaging/detection sensor—Part I: System setup and experimental evaluations," *IEEE Sensors J.*, vol. 20, no. 18, pp. 10824–10832, Sep. 2020.
- [33] D. M. Sheen and T. E. Hall, "Calibration, reconstruction, and rendering of cylindrical millimeter-wave image data," *Proc. SPIE*, vol. 8022, May 2011, Art. no. 80220H.
- [34] D. M. Sheen, "Sparse multi-static arrays for near-field millimeter-wave imaging," in *Proc. IEEE Global Conf. Signal Inf. Process.*, Austin, TX, USA, Dec. 2013, pp. 699–702.
- [35] D. M. Sheen and T. E. Hall, "Reconstruction techniques for sparse multistatic linear array microwave imaging," *Proc. SPIE*, vol. 9078, Jun. 2014, Art. no. 90780I.
- [36] D. A. Wikner, J. L. Fernandes, J. R. Tedeschi, D. M. Sheen, D. L. McMakin, and A. R. Luukanen, "Three-dimensional millimeter-wave imaging for concealed threat detection in shoes," *Proc. SPIE*, vol. 8715, May 2013, Art. no. 87150C.
- [37] X. Zhuge and A. G. Yarovoy, "A sparse aperture MIMO-SAR-Based UWB imaging system for concealed weapon detection," *IEEE Trans. Geosci. Remote Sens.*, vol. 49, no. 1, pp. 509–518, Jan. 2011.
- [38] X. Zhuge and A. G. Yarovoy, "Three-dimensional near-field MIMO array imaging using range migration techniques," *IEEE Trans. Image Process.*, vol. 21, no. 6, pp. 3026–3033, Jun. 2012.
- [39] J. Gao, Y. Qin, B. Deng, H. Wang, and X. Li, "A novel method for 3-D millimeter-wave holographic reconstruction based on frequency interferometry techniques," *IEEE Trans. Microw. Theory Techn.*, vol. 66, no. 3, pp. 1579–1596, Mar. 2018.
- [40] J. Gao, B. Deng, Y. Qin, H. Wang, and X. Li, "An efficient algorithm for MIMO cylindrical millimeter-wave holographic 3-D imaging," *IEEE Trans. Microw. Theory Techn.*, vol. 66, no. 11, pp. 5065–5074, Nov. 2018.
- [41] M. E. Yanik and M. Torlak, "Near-field MIMO-SAR millimeter-wave imaging with sparsely sampled aperture data," *IEEE Access*, vol. 7, pp. 31801–31819, 2019.
- [42] M. Ravan, R. K. Amineh, and N. K. Nikolova, "Two-dimensional near-field microwave holography," *Inverse Problems*, vol. 26, no. 5, May 2010, Art. no. 055011.
- [43] R. K. Amineh, M. Ravan, A. Khalatpour, and N. K. Nikolova, "Three-dimensional near-field microwave holography using reflected and transmitted signals," *IEEE Trans. Antennas Propag.*, vol. 59, no. 12, pp. 4777–4789, Dec. 2011.
- [44] R. K. Amineh, J. J. McCombe, A. Khalatpour, and N. K. Nikolova, "Microwave holography using point-spread functions measured with calibration objects," *IEEE Trans. Instrum. Meas.*, vol. 64, no. 2, pp. 403–417, Feb. 2015.
- [45] D. Tajik, F. Foroutan, D. S. Shumakov, A. D. Pitcher, and N. K. Nikolova, "Real-time microwave imaging of a compressed breast phantom with planar scanning," *IEEE J. Electromagn., RF Microw. Med. Biol.*, vol. 2, no. 3, pp. 154–162, Sep. 2018.
- [46] R. K. Amineh, N. K. Nikolova, and M. Ravan, *Real-Time Three-Dimensional Imaging of Dielectric Bodies Using Microwave/Millimeter Wave Holography*. Piscataway, NJ, USA: Wiley, 2019.
- [47] N. K. Nikolova, *Introduction to Microwave Imaging*. Cambridge, U.K.: Cambridge Univ. Press, 2017.
- [48] J. Li, H. Wang, X. Wang, Y. Yan, and H. Donglin, "Comparative study on stepped frequency pulsed and continuous wave SARs," *Radar Sci. Technol.*, vol. 14, no. 1, pp. 45–53, 2016.
- [49] D. Cherniak and S. Levantino, "Chirp generators for millimeter-wave FMCW radars," in *Special Topics in Information Technology*. Cham, Switzerland: Springer, 2020, ch. 3, pp. 33–47.
- [50] J. Zhang, "Study on imaging algorithms and parameters estimation methods for FMCW SAR," M.S. thesis, College Electron. Inf. Eng., Nanjing Univ. Aeronaut. Astronaut., Nanjing, China, 2011.
- [51] D. Bleh *et al.*, "W-band time-domain multiplexing FMCW MIMO radar for far-field 3-D imaging," *IEEE Trans. Microw. Theory Techn.*, vol. 65, no. 9, pp. 3474–3484, Sep. 2017.
- [52] Y. Nan, X. Huang, and Y. J. Guo, "A millimeter-wave GCW-SAR based on Deramp-on-Receive and piecewise constant Doppler imaging," *IEEE Trans. Geosci. Remote Sens.*, vol. 58, no. 1, pp. 680–690, Jan. 2020.
- [53] T. Geibig, A. Shokhetbrod, A. Hommes, R. Herschel, and N. Pohl, "Compact 3D imaging radar based on FMCW driven frequency-scanning antennas," in *Proc. IEEE Radar Conf. (RadarConf)*, Philadelphia, PA, USA, May 2016, pp. 1–5.
- [54] D. M. Sheen, B. E. Bernacki, and D. L. McMakin, "Advanced millimeter-wave security portal imaging techniques," *Proc. SPIE*, vol. 8259, Feb. 2012, Art. no. 82590G.
- [55] Cumming, Ian G. and Frank H. Wong, *Digital Processing of Synthetic Aperture Radar Data: Algorithms and Implementation*. Boston, MA, USA: Artech House, 2005.
- [56] G. A. Mastin, *Algorithm Architecture for Synthetic Aperture Radar (SAR) Ground Processing*. Accessed: Mar. 20, 2020. [Online]. Available: <https://math.la.asu.edu/~kuang/LM/031014.pdf>
- [57] A. W. Doerry, "Basics of polar-format algorithm for processing synthetic aperture radar images," Sandia Nat. Laboratories, Livermore, CA, USA, Sandia Rep. SAND2012-3369, 2012. [Online]. Available: <https://prodng.sandia.gov/techlib/noauth/access-control.cgi/2012/123369.pdf>
- [58] Y. Meng, C. Lin, J. Zang, and A. Qing, "MMW holographic imaging for security check," in *Proc. IEEE Asia-Pacific Microw. Conf. (APMC)*, Singapore, Dec. 2019, pp. 569–571.
- [59] E. Goldstein and M. Katzen, "On Weyl's identity," *Annali di Matematica Pura ed Applicata*, vol. 87, no. 1, pp. 287–298, 1970.
- [60] K. Aki and P. G. Rechards, *Quantitative Seismology*. Sausalito, CA, USA: Univ. Science Books, 2002.
- [61] M. Ayatollahi and S. Safavi-Naeini, "A new representation for the Green's function of multilayer media based on plane wave expansion," *IEEE Trans. Antennas Propag.*, vol. 52, no. 6, pp. 1548–1557, Jun. 2004.
- [62] D. M. Chandler, "Seven challenges in image quality assessment: Past, present, and future research," *ISRN Signal Process.*, vol. 2013, pp. 1–53, 2013.
- [63] I. H. Shahrezaei, M. Kazerooni, and M. Fallah, "A total quality assessment solution for synthetic aperture radar nlfm waveform generation and evaluation in a complex random media," *Int. J. Smart Sens. Intell. Syst.*, vol. 10, no. 1, pp. 174–198, 2017.

- [64] D. Kettler, N. Redding, and D. Gray, "Exact point spread functions for SAR imaging," in *Proc. Committee Earth Observ. Satell., Synth. Aperture Radar Workshop*, 2005, pp. 1–8.
- [65] U. K. Majumder, M. A. Temple, M. J. Minardi, and E. G. Zelnio, "Point spread function characterization of a radially displaced scatterer using circular synthetic aperture radar," in *Proc. IEEE Radar Conf.*, Boston, MA, USA, Apr. 2007, pp. 729–733.
- [66] M. Elsaadouny, J. Barowski, and I. Rolfes, "Millimeter wave short range SAR imaging using cross-polarized radar system," in *Proc. IEEE 9th Annu. Inf. Technol., Electron. Mobile Commun. Conf. (IEMCON)*, Vancouver, BC, Canada, Nov. 2018, pp. 475–478.
- [67] J. Moll, P. Schöps, and V. Krozer, "Towards three-dimensional millimeter-wave radar with the bistatic fast-factorized back-projection algorithm—Potential and limitations," *IEEE Trans. Terahertz Sci. Technol.*, vol. 2, no. 4, pp. 432–440, Jul. 2012.
- [68] J. Zhang, Y. Fu, W. Zhang, and W. Yang, "Signal characteristics analysis and intra-pulse motion compensation for FMCW CSAR," *IEEE Sensors J.*, vol. 19, no. 22, pp. 10461–10476, Nov. 2019.
- [69] J. Barber *et al.*, "Developing an ANSI standard for image quality tools for the testing of active millimeter wave imaging systems," *Proc. SPIE*, vol. 10189, May 2017, Art. no. 1018905.
- [70] J. Barber *et al.*, "Thin film partial reflectors for generating contrast in millimeter wave images," *Proc. SPIE*, vol. 10634, May 2018, Art. no. 106340I.
- [71] Z. Wang, A. C. Bovik, H. R. Sheikh, and E. P. Simoncelli, "Image quality assessment: From error visibility to structural similarity," *IEEE Trans. Image Process.*, vol. 13, no. 4, pp. 600–612, Apr. 2004.
- [72] S. Hu, X. Wang, and Q. Si, "Effects of FM linearity of linear FM signals on pulse-compression performance," in *Proc. CIE Int. Conf. Radar*, Shanghai, China, Oct. 2006, pp. 1–5.
- [73] *MATLAB R2017a*, The MathWorks, Natick, MA, USA, 2007.



**Yang Meng** received the B.E. degree in electronic information science and technology from the Chongqing University of Arts and Sciences, Chongqing, China, in 2014. He is currently pursuing the Ph.D. degree in radio physics with the University of Electronic Science and Technology of China, Chengdu, China, under the supervision of Prof. Anyong Qing.

From September 2019, he has been an International Visiting Ph.D. Student with the Department of Electrical and Computer Engineering, McMaster University, Hamilton, ON, Canada, under the supervision of Prof. Natalia K. Nikolova. His research interests include the areas of millimeter-wave imaging, electromagnetic scattering, and inverse scattering.



**Chuan Lin** (Member, IEEE) received the B.Eng. and Ph.D. degrees from Southwest Jiaotong University, Chengdu, China, in 2003 and 2009, respectively. He joined the Southwest Research Institute of Electronic Equipment, Chengdu, China, as an Engineer, in April 2010, and a Senior Engineer in 2012. From May 2013 to April 2017, he was an Associate Professor with the University of Electronic Science and Technology of China, Chengdu. He is currently an Associate Professor with Southwest Jiaotong University, Chengdu. His research interests include terahertz and millimeter-wave imaging, antenna arrays, computational intelligence, and pattern recognition.

Dr. Lin is a Reviewer for several international journals, such as *IEEE TRANSACTIONS ON ANTENNAS AND PROPAGATION*, *IET Image Processing*, *IET Microwaves, Antennas & Propagation*, and *Journal of Applied and Numerical Optimization*.



**Jiefeng Zang** received the Ph.D. degree in electromagnetic field and electromagnetic wave from Southwest Jiaotong University, Chengdu, China, in 2009.

His research work is mainly focused on millimeter wave imaging and image processing.



**Anyong Qing** (Senior Member, IEEE) was born in Hunan, China, in May 27, 1972. He received the B.E. degree in electromagnetic theory and microwave technology from Tsinghua University, Beijing, China, in 1993, the M.E. degree in electromagnetic theory and microwave technology from the Beijing Broadcasting Institute, Beijing, in 1995, and the Ph.D. degree in electromagnetic theory and microwave technology from Southwest Jiaotong University, Chengdu, China, in 1997.

He was a Post-Doctoral Fellow with the Department of Communication Engineering, Shanghai University, Shanghai, China, from September 1997 to June 1998 and a Research Fellow at the School of Electrical and Electronic Engineering, Nanyang Technological University, Singapore, from June 1998 to June 2000. He was a Member of Scientific Staff with the Electromagnetic Theory Group, Department of Electrical Engineering, University of Kassel, Kassel, Germany, from July 2000 to May 2001. He was a Research Scientist at Temasek Laboratories, National University of Singapore, Singapore, from September 2001 to December 2009 and a Senior Research Scientist from January 2010 to October 2012. He was a Professor with the School of Physics, University of Electronic Science and Technology of China, Chengdu, since November 2012(part time since December 2017). He is currently a Chair with the Department of Electrical Electronics, Southwest Jiaotong University. His research interests include terahertz theory and technology, photoacoustic theory and technology, compressive sensing, natural optimization, computational acoustics and electromagnetics, inverse acoustic and electromagnetic scattering, electromagnetic composite materials, antennas and antenna arrays, millimeter wave and terahertz imaging, and biomedical imaging.

Dr. Qing was granted National Young Thousand Talent professorship in September 2011. He is a member of the Material Research Society Singapore and the Chinese Institute of Electronics. He has been an Associate Editor of the *Radio Science* since 2017.



**Natalia K. Nikolova** (Fellow, IEEE) received the Dipl.Eng. degree from the Technical University of Varna, Bulgaria, in 1989, and the Ph.D. degree from the University of Electro-Communications, Tokyo, Japan, in 1997.

From 1998 to 1999, she held a Post-Doctoral Fellowship of the Natural Sciences and Engineering Research Council of Canada (NSERC), during which time she was initially with the Microwave and Electromagnetics Laboratory, DalTech, Dalhousie University, Halifax, NS, Canada, and, later, for a year, with the Simulation Optimization Systems Research Laboratory, McMaster University, Hamilton, ON, Canada. In July 1999, she joined the Department of Electrical and Computer Engineering, McMaster University, where she is currently a Professor. Her research interests include inverse scattering and microwave imaging, theoretical and computational electromagnetism, as well as high-frequency computer-aided design.

Dr. Nikolova was a recipient of a University Faculty Award of NSERC from 2000 to 2005. From 2008 to 2018, she held a Canada Research Chair in High-frequency Electromagnetics. She is a Fellow of the Canadian Academy of Engineering (CAE).